Available online at www.sciencedirect.com
SCIENCE DIRECT®
Icarus 173 (2005) 508–521
ICARUS
www.elsevier.com/locate/icarus

HST observations of spokes in Saturn's B ring

Colleen A. McGhee [a,*], Richard G. French [a], Luke Dones [b], Jeffrey N. Cuzzi [c], Heikki J. Salo [d], Rebecca Danos [e]

[a] *Astronomy Department, Wellesley College, Wellesley, MA 02481, USA*
[b] *Southwest Research Institute, Boulder, CO 80302, USA*
[c] *NASA Ames Research Center, Moffett Field, CA 94035, USA*
[d] *University of Oulu, Astronomy Division, PO Box 3000, Oulu, Finland*
[e] *Department of Physics and Astronomy, UCLA, Los Angeles, CA, 90095-1547, USA*

Received 11 June 2004; revised 31 August 2004

Available online 11 November 2004

Abstract

As part of a long-term study of Saturn's rings, we have used the Hubble Space Telescope's (HST) Wide Field and Planetary Camera (WFPC2) to obtain several hundred high resolution images from 1996 to 2004, spanning the full range of ring tilt and solar phase angles accessible from the Earth. Using these multiwavelength observations and HST archival data, we have measured the photometric properties of spokes in the B ring, visible in a substantial number of images. We determined the spoke particle size distribution by fitting the wavelength-dependent extinction efficiency of a prominent, isolated spoke, using a Mie scattering model. Following Doyle and Grün (1990, Icarus 85, 168–190), we assumed that the spoke particles were sub-micron size spheres of pure water ice, with a Hansen–Hovenier size distribution (Hansen and Hovenier, 1974, J. Atmos. Sci. 31, 1137–1160). The WFPC2 wavelength coverage is broader than that of the Voyager data, resulting in tighter constraints on the nature of spoke particles. The effective particle size was $r_{\rm eff} = 0.57 \pm 0.05$ μm, and the size distribution was quite narrow with a variance of $b = 0.09 \pm 0.03$, very similar to the results of Doyle and Grün (1990, Icarus 85, 168–190), and consistent with predictions of plasma cloud models for spoke production from meteoritic impacts (Goertz and Morfill, 1983, Icarus 53, 219–229; Goertz, 1984, Adv. Space Res. 4, 137–141). In all, we identified 36 spokes or spoke complexes, predominantly on the morning (east) ansa. The photometric contrast of the spokes is strongly dependent on effective ring opening angle, $B_{\rm eff}$. Spokes were clearly visible on the north face of the rings in 1994, just prior to the most recent ring plane crossing (RPX) epoch, and on the south face shortly after RPX. However, spokes were both less abundant and fainter as the rings opened up, and no spokes were detected after 18 October 1998 ($B_{\rm eff} = -15.43°$), when a single faint spoke was seen on the morning ansa. The high resolution and photometric quality of the WFPC2 images enabled us to set a detection limit of $\leqslant 1\%$ in fractional brightness contrast for spokes for the post-1998 observations. We compare the observed trend of spoke contrast with $B_{\rm eff}$ to radiative transfer calculations based on three models of the distribution of spoke material. In the first, the spoke "haze" is uniformly mixed with macroscopic B ring particles. No variation in spoke contrast is predicted for single-scattering, in this case, and only a modest decrease in contrast with $B_{\rm eff}$ is predicted when multiple scattering is taken into account. In the second model, the spoke dust occupies an extended layer that is thicker than the B ring, which gives virtually identical results to a third case, when the haze layer lies exclusively above the ring. Multiple-scattering Monte Carlo calculations for these two extended haze models match the trend of spoke contrast exceptionally well. We compute the predicted spoke contrast for a wide variety of viewing geometries, including forward- and backscattering. Based on these results, spokes should be easily detectable during the Cassini mission when the rings are viewed at relatively small ($|B| \leqslant 10°$) ring opening angles.

Keywords: Planetary rings, Saturn; Radiative transfer

* Corresponding author.
E-mail address: cmcghee@wellesley.edu (C.A. McGhee).

0019-1035/$ – see front matter
doi:10.1016/j.icarus.2004.09.001

1. Introduction

Spokes, the wispy ephemeral features in Saturn's B ring, were first seen clearly in Voyager 1 images taken during its flyby of the Saturn system in 1980 (Collins et al., 1980). Although groundbased observers had reported seeing streaks in the A ring as early as 1873 (Alexander, 1962) and had even computed a rotational period for features seen in the B ring in the 1970s (Robinson, 1980), the B ring's vast panorama of spokes seen in the Voyager images was unexpected. In response to this and other ring discoveries, the Voyager 2 observing strategy was altered to be able to take a closer and better look at the ring system (Smith et al., 1982), resulting in extensive coverage of spokes during the 1981 flyby.

The picture that has emerged from the Voyager observations is that spokes are made up of fine dust particles, interacting with Saturn's magnetic field, and triggered by meteoritic impacts with the rings (Goertz and Morfill, 1983). Other mechanisms have also been proposed, such as photoionization of dust particles that would then be charged and lifted out of the ring plane, and magnetic field-aligned currents aligning small particles (Gold, 1980; Bastin, 1981; Hill and Mendis, 1981; Carbary et al., 1982; Davydov, 1982; Mendis et al., 1984; Connerney, 1986; Tagger et al., 1991). The fact that spokes were darker than the rings at visible wavelengths as Voyager 1 approached Saturn (backscattered light), but brighter than the rings when the spacecraft turned to look more into the Sun (forward scattered light) after close encounter, suggested that the spokes were made of very small, roughly micron-sized particles (Smith et al., 1981). Doyle et al. (1989) concluded from radiative transfer modeling that spoke-free B ring regions contained very little free submicron dust. Subsequently, Doyle and Grün (1990) used Voyager multicolor broadband photometry of seven spokes to constrain spoke particle sizes. They found a relatively narrow size distribution, with a peak at effective radius $r_{\rm eff} = 0.6 \pm 0.2$ μm. This is consistent with theoretical calculations of Goertz and Morfill (1983) and Goertz (1984), who developed a model for spoke formation from a plasma cloud produced by a meteoritic impact. The probability of capture of at least one charge by a dust grain increases with the particle cross-section, but large grains are too massive to levitate quickly off the rings. This sets lower and upper bounds on the spoke particle size, centered on $r_{\rm eff} = 0.5$ μm. On the other hand, Meyer-Vernet (1984) identified a number of complicating electromagnetic effects, such as spin destruction of grains and the electrostatic attraction between the spoke grain and the much larger parent ring particle (see Doyle, 1987, for a review). An accurate determination of the spoke particle size distribution provides an important constraint on models of spoke production and evolution.

Here, we report on an extensive set of observations of spokes taken with the Hubble Space Telescope (HST). Spokes had remained virtually unobserved since the 1980 and 1981 Voyager flybys until 1994, when the HST's Wide Field and Planetary Camera (WFPC2) first targeted Saturn (Beebe, HST program ID 5776).[1] In 1996, we began a long-term program using WFPC2 to observe the rings, atmosphere, and satellites at each opposition over a full Saturn season. Our observations began just after the most recent ring plane crossing (RPX) epoch in 1995 (the onset of southern spring on Saturn). They extended through March 2004, shortly after southern summer, when the rings had reached their most open extent as seen from the Sun and Earth, and just prior to the Cassini orbital tour. The superb image quality of the HST has enabled us to detect spokes in many WFPC2 images and to measure their contrast relative to the nearby spoke-free regions. When the rings were nearly edge-on, spokes were abundant and clearly visible on the north side of the rings (prior to RPX) and on the south (after RPX). As the rings opened up, the spoke contrast decreased, and eventually spokes became undetectable. The photometric precision and uniformity of the observations enabled us to set stringent detection limits on the maximum spoke optical depth as the ring opening angle varied over the course of a full Saturn season. In Section 2, we describe our observations and present our measurements of spoke contrast. In Section 3, we determine the particle size distribution for a single well-isolated spoke by measuring the wavelength dependence of the extinction efficiency. We discuss our spoke detection limits in Section 4, and compare the observations with radiative transfer calculations for three models of the distribution of spoke material. In the final section, we summarize our results.

2. Observations

For this investigation of Saturn's B ring spokes, our primary observations are from our 1996–2004 WFPC2 program to observe the rings over the full range of ring tilt and phase angles accessible from the Earth. During most of our allocated HST orbits (or "visits"), we imaged the east (morning) and west (evening)[2] ring ansae separately in the high-resolution PC chip, in each of the five WFPC2 wideband UBVRI filters (F336W, F439W, F555W, F675W, and F814W), and occasionally in the F255W, F785LP, and F1042M filters. Exposures were separated by about three minutes. For completeness, we searched the entire HST data archive for WFPC2 images of spokes on the illuminated face of Saturn's rings. Table 1 summarizes the full set of observations used in this paper. For each data set, identified by HST program ID number, we list the date of each visit, the ring plane opening angle as viewed from the Earth (B) and

[1] A visual detection of spokes using the Pic du Midi 1-m telescope was reported by Sheehan and O'Meara (1993), and spokes were observed in CCD images taken in November and December, 1994 from Pic du Midi (Colas et al., 1995).

[2] We adopt the astronomical convention for east and west as measured from Earth in the plane of the sky, relative to Saturn's center.

Table 1
HST observations

Prog. ID	Date	B (°)	B' (°)	B_{eff} (°)	α (°)	# spokes		$-\frac{\Delta(I/F)}{(I/F)_B}$ [a]	
						E	W	E	W
5776	1994 Dec 1	7.89	5.18	6.25	5.84	3	2	0.097	[b]
6806	1996 Sep 30	−4.31	−4.73	−4.51	0.46	3	3	0.120	0.078
6806	1996 Oct 14	−3.82	−4.93	−4.30	1.93	5	3	0.161	0.052
6806	1997 Jan 10	−3.72	−6.25	−4.66	5.67	1	1	0.134	0.089
7427	1997 Sep 22	−10.59	−10.01	−10.29	2.00	0	1	[b]	0.079
7427	1997 Oct 1	−10.28	−10.15	−10.21	0.98	2	0	0.044	[b]
7427	1997 Oct 6	−10.12	−10.22	−10.17	0.50	6	2	0.054	0.042
7427	1997 Oct 10	−9.99	−10.28	−10.13	0.30	2	0	0.032	[b]
7427	1998 Jan 1	−8.88	−11.47	−10.01	6.02	1	0	0.013	[b]
7427	1998 Jul 28	−16.67	−14.38	−26.72	6.26	0	0	(0.012)	(0.012)
7427	1998 Oct 13	−15.57	−15.42	−26.72	1.20	0	0	(0.009)	(0.009)
7427	1998 Oct 18	−15.43	−15.47	−15.45	0.69	1	0	0.027	(0.009)
7427	1998 Oct 24	−15.25	−15.56	−26.71	0.32	0	0	(0.008)	(0.008)
8398	1999 Aug 25	−21.05	−19.36	−26.71	6.11	0	0	(0.011)	(0.011)
8398	1999 Nov 3	−19.98	−20.16	−26.71	0.43	0	0	(0.008)	(0.008)
8398	1999 Nov 7	−19.90	−20.20	−25.75	0.30	0	0	(0.008)	(0.008)
8660	2000 Aug 4	−24.19	−22.92	−25.61	6.10	0	0	(0.011)	(0.011)
8660	2000 Nov 20	−23.56	−23.83	−25.59	0.27	0	0	(0.008)	(0.008)
8660	2000 Nov 24	−23.50	−23.85	−23.68	0.59	0	0	(0.008)	(0.008)
8660	2000 Dec 6	−23.33	−23.96	−23.64	1.99	0	[c]	(0.009)	[c]
8802	2001 Sep 8	−26.16	−25.71	−25.93	6.37	0	0	(0.011)	(0.011)
8802	2001 Nov 28	−25.90	−26.07	−25.99	0.62	0	0	(0.008)	(0.008)
8802	2002 Jan 31	−25.76	−26.29	−26.03	5.58	0	0	(0.010)	(0.010)
9341	2002 Sep 21	−26.37	−26.73	−26.55	6.38	0	0	(0.011)	(0.010)
9341	2002 Nov 30	−26.47	−26.72	−26.59	2.01	0	0	(0.009)	(0.009)
9341	2002 Dec 9	−26.52	−26.72	−26.62	1.00	0	0	(0.009)	(0.009)
9341	2002 Dec 14	−26.55	−26.71	−26.63	0.40	0	0	(0.008)	(0.008)
9341	2002 Dec 16	−26.56	−26.71	−26.64	0.23	0	0	(0.008)	(0.008)
9341	2002 Dec 17	−26.57	−26.71	−26.64	0.15	0	0	(0.007)	(0.007)
9809	2003 Aug 25	−25.41	−26.17	−25.79	5.05	0	0	(0.010)	(0.010)
9809	2003 Dec 5	−25.11	−25.75	−25.42	3.05	0	0	(0.009)	(0.009)
9809	2003 Dec 31	−25.53	−25.61	−25.57	0.08	0	0	(0.007)	(0.007)
9809	2004 Jan 1	−25.54	−25.61	−25.58	0.10	0	0	(0.007)	(0.007)
9809	2004 Jan 5	−25.60	−25.59	−25.60	0.50	0	0	(0.008)	(0.008)

[a] The normalized contrast of the darkest spoke observed with the F555W filter on each date. Entries in parentheses detection limits, in cases where no spokes were visible.
[b] Accurate photometry was not possible on spokes in these images.
[c] No west ansa images were taken on this date.

the Sun (B'), and the solar phase angle α, as well as other quantities to be defined later.

We used standard pipeline-processed images for our analysis. The geometric and photometric calibrations of our PC images, and details about individual observations, are described in detail by Cuzzi et al. (2002), Poulet et al. (2002), and French et al. (2003). Briefly summarized, we corrected each image for geometric distortion using the Trauger et al. (1995) transformation, and determined the global coordinates of Saturn's center and the absolute ring plane radius scale by fitting the Encke Division in each image. We converted from data number (DN) to reflectivity I/F by integrating in wavelength over the product of the solar spectrum and the detector and filter response, as described by Nicholson et al. (1996). The remarkable quality of the WFPC2 images is evident in Fig. 1, which shows a spoke complex near elongation on the morning (east) ansa, taken on 30 September 1996, with a ring opening angle B of only −4.31°. The spoke region, magnified in the inset box, is unsharp-masked to accentuate the contrast. In Fig. 2, both the east and west ansae are reprojected to show the true shape of the spokes. Since even the diffraction-limited HST images have finite resolution, the strong foreshortening of the rings at this viewing angle changes the radial resolution as a function of longitude relative to elongation. In this figure, the morning and evening (east and west) ansae F555W images of 30 September 1996 were stretched in the north–south direction by $1/\sin|B|$ to give a bird's-eye view of the rings. The top row shows the images with linear contrast, and the bottom row shows them unsharp-masked. The original, unstretched images are shown at left in each panel. Notice that the Encke and Cassini Divisions are well-resolved at elongation, but the radial resolution degrades rapidly away from elongation. The unsharp masked morning ansa images (lower left) clearly reveal several spoke complexes. On the

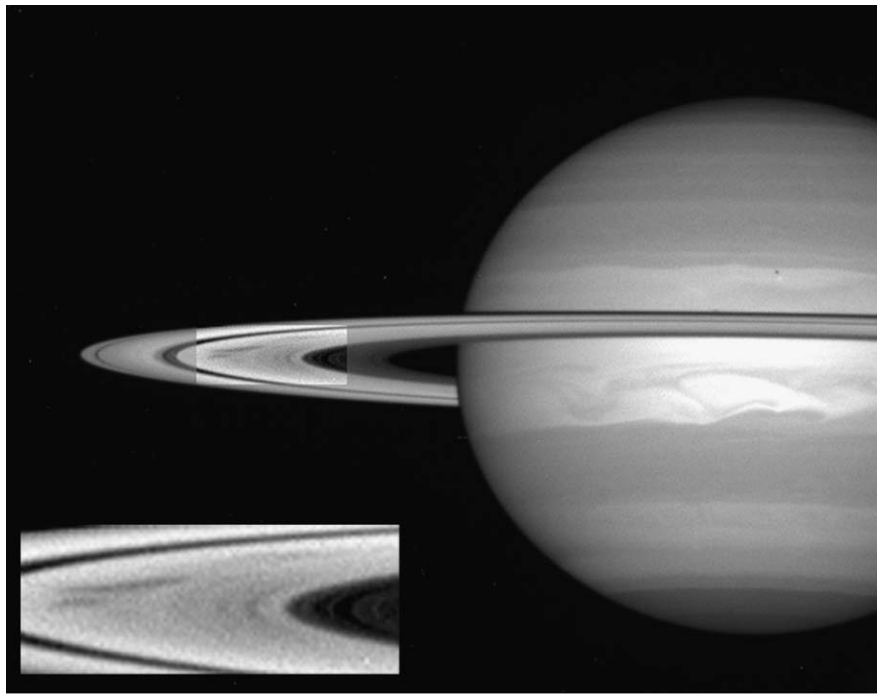

Fig. 1. Spokes on the south face of Saturn's B ring are clearly seen in this F555W WFPC2 image (data set ID u3ic0403t) of the morning (east) ansa, taken on 30 September 1996. The highlighted region, magnified in the lower left, has been unsharp-masked to accentuate the contrast.

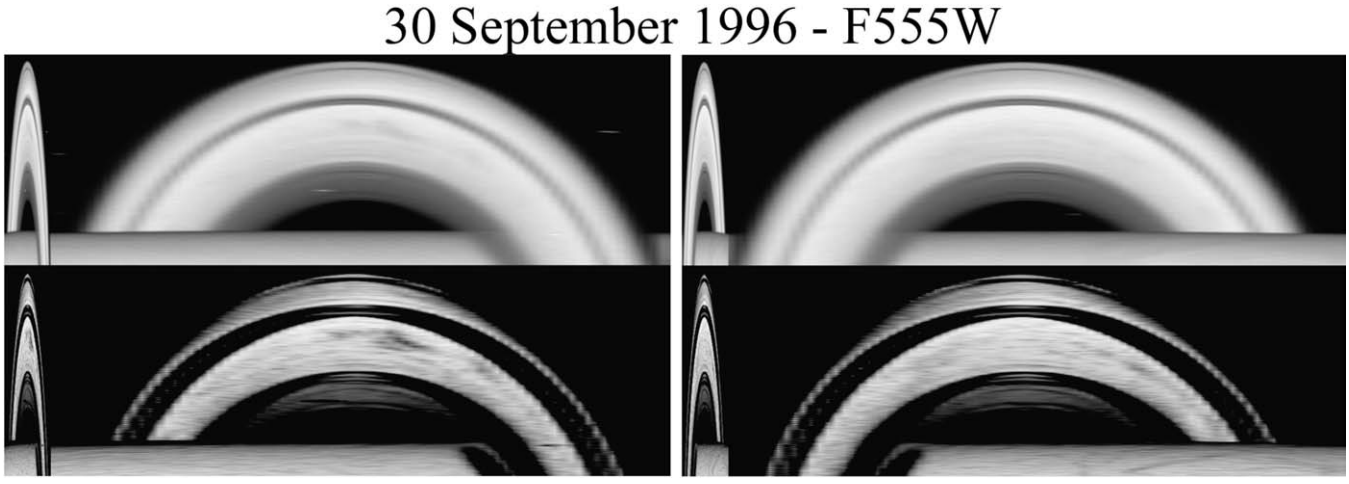

Fig. 2. The true shape of the spokes shown in Fig. 1 is most easily seen by reprojecting the image, as shown in the left column. The morning ansa image has been spatially stretched to give a bird's-eye view of the ring system. The upper left panel shows the original data, while the lower left panel is unsharp-masked. Also included, in the right column, is the corresponding F555W image from the evening (west) ansa (data set ID u3ica402t). Faint spokes are visible here as well.

evening (west) ansa, spokes are also present, although more muted in contrast.

2.1. Measuring spoke contrast

To characterize spoke particle properties, we measured the spoke brightnesses relative to the nearby rings. We define the normalized spoke contrast as

$$\frac{\Delta(I/F)}{(I/F)_{\rm B}} = \frac{(I/F)_{\rm spoke} - (I/F)_{\rm B}}{(I/F)_{\rm B}}, \qquad (1)$$

where $(I/F)_{\rm spoke}$ is the reflectivity of the spoke and $(I/F)_{\rm B}$ is the reflectivity of spoke-free B ring at the same orbital radius. At the solar phase angles accessible from the Earth, $(I/F)_{\rm spoke} < (I/F)_{\rm B}$, in which case spokes are darker than the B ring and the spoke contrast is < 0. Ideally, we would use a second, spoke-free image of the rings, taken with the same viewing geometry and filter, as a measure of the spoke-free $(I/F)_{\rm B}$. Unfortunately, such multiple images were not taken in the early years of our HST program, and we have adopted two other strategies to measure the background B ring brightness. One is to reflect the image about the long

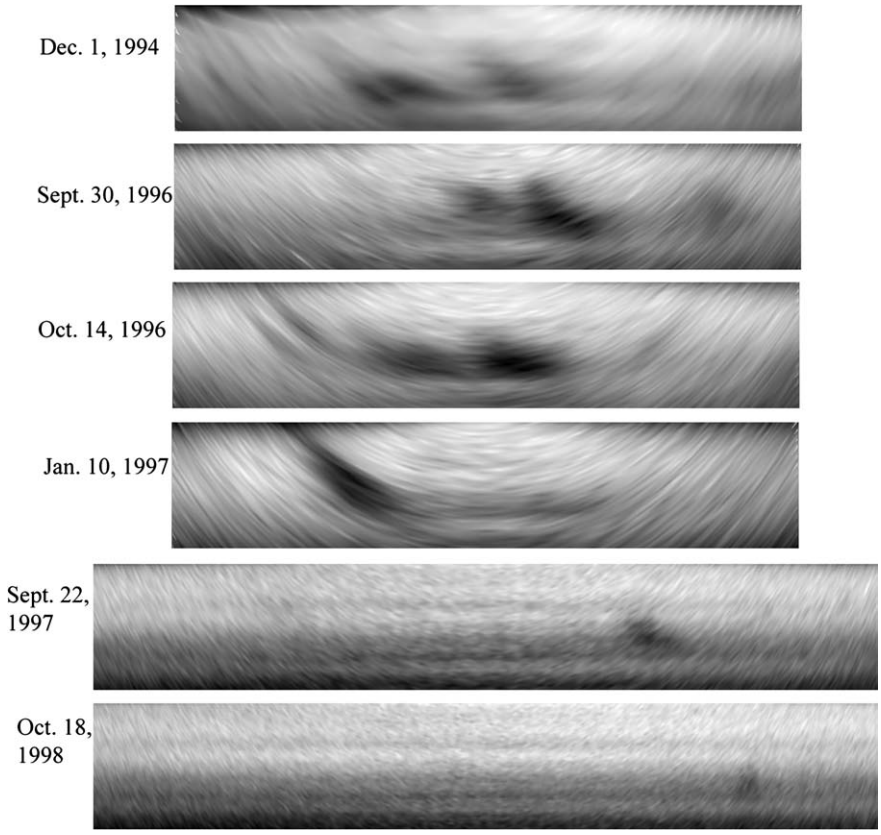

Fig. 3. Images of spokes, reprojected onto a rectangular coordinate system with radius increasing upward from 100,000 to 116,000 km in each strip, and orbital longitude increasing to the right, centered on elongation, and compressed by a factor of 1.75 relative to the vertical axis. The 1 December 1994 F547M east ansa image was taken in the wide-field chip of the WFPC2. All others are F555W PC images of the east ansa, except as noted. From top to bottom, images are data set IDs u2kr0105t, u3ic0403t, u3ic0203t, u3ic0103t, u46a0209r (west ansa), and u46a7203r.

axis of the rings to produce a mirror image. Then, for a spoke in the trailing east quadrant, we could use the leading east quadrant in the mirror image as a comparison region, which would be affected in exactly the same way as the spoke region by diffraction and longitudinally variable radial resolution. Of course, this requires that the mirrored region is spoke-free. In cases where spokes are present in both the leading and trailing quadrants, we have used the leading or trailing quadrant on the opposite ansa (if such images exist) as a comparison region, when either of these regions is spoke-free.

We reprojected all of our images onto a rectangular coordinate system of radius r and ring longitude θ, measured in a prograde direction from the sub-observer point on the near ring. To preserve photometric accuracy, we subdivided each image pixel into 20×20 subpixels and mapped them into bins of radial extent $dr = 100$ km and longitudinal width $d\theta = 0.1°$. (At $r = 100{,}000$ km, $r\,d\theta = 175$ km. Note that a PC image has a scale of $0.0455''/\text{px} \simeq 300$ km at Saturn, so that our transformation preserves the resolution of the original images.) This reprojection puts all images on a common scale, making it easy to subtract one from another, or to reverse and subtract a mirror image from the image itself. It also makes it possible to correct for Keplerian shear between successive exposures by evolving each image back to a common epoch, using the known radial dependence of the orbital mean motion.

Figure 3 shows (r, θ) reprojections of representative spokes in the outer B ring from 1994–1998, with the effective ring opening angle B_{eff} between $+6.25°$ in 1994 and $-15.45°$ in 1998, where

$$\sin B_{\text{eff}} = \frac{2 \sin B \sin B'}{\sin B + \sin B'}. \tag{2}$$

Table 1 lists B_{eff} for all of our observations. The vertical axis of each strip extends upward from $r = 100{,}000$ km to $r = 116{,}000$ km. The horizontal axis is centered at elongation, compressed by a factor of 1.75 relative to the vertical axis. Note the abundance of high contrast spokes in the first four images, all taken at low B_{eff}. At larger ring opening angles, spokes were fainter and rarer. The last spoke detected in our HST images was observed on 18 October 1998 ($B_{\text{eff}} = -15.45°$). No other spokes were visible in the subsequent 5.5 years.

2.2. Corrections for orbital motion

During each HST visit, we cycled through a variety of filters for each ansa. Although most exposures were quite short, WFPC2 requires three minutes to change filters and

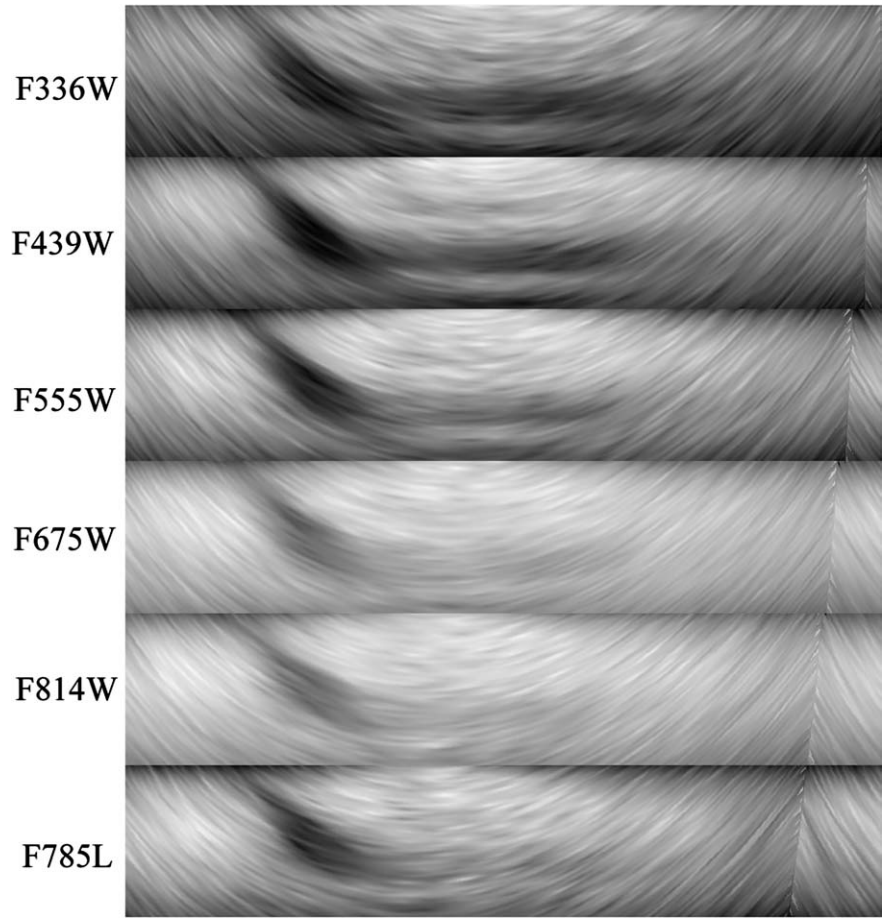

Fig. 4. A prominent, isolated spoke was observed on the east ansa on 10 June 1997 in six broadband filters. The successive images have been reprojected and then corrected for differential orbital motion by evolving each image to the epoch of the earliest (F336W) exposure. Notice that the shape and location of the spoke change very little in these evolved projections, which span a total of $\sim$ 15 minutes. From top to bottom, the images are data set IDs u3ic0101t, u3ic0102t, u3ic0103t, u3ic0104t, u3ic0105t, and u3ic0106p.

prepare for the next image, so that typically 15–20 minutes elapsed between the first and last image of a set. Over this interval, the spoke appears to move, through a combination of Keplerian shear and any intrinsic ring-relative motion. Grün et al. (1992) measured the angular velocity of spoke edges from high-resolution Voyager image pairs taken 24 minutes apart (comparable to the total duration of our HST image sets). They found that deviations from Keplerian orbital motion were quite small, and typically less than 5×10^{-6} rad/s, or about 600 km in the azimuthal direction during 24 minutes, compared with $\sim$ 30,000 km of orbital motion during the same interval. Since a single PC pixel at elongation has a longitudinal extent of about 300 km/ $\sin|B| \gg$ 600 km, any differences between actual spoke motion and Keplerian motion in our HST images would be evident only at the subpixel level, and we can safely ignore them.

As an illustration of the effectiveness of correcting for orbital motion, Fig. 4 shows a sequence of six spoke images, taken on 10 January 1997, evolved to the epoch of the first exposure in the set, taken in the F336W filter. Notice that the prominent spoke at the left is in the same location of each evolved image. The "sutures" at the right show the radially-variable longitude shift introduced to correct for Keplerian shear.

3. Spoke particle sizes

The most extensive prior color analysis of Voyager images of spokes was performed by Doyle and Grün (1990), who estimated the particle size distribution of the spokes from their wavelength-dependent extinction efficiency. The Voyager clear filter observations over a range of phase angles had previously been modeled using a Henyey–Greenstein phase function and indicated a particle size $r_{\rm eff} \geqslant 0.15$ μm (Doyle et al., 1989). Four-color photometry of spokes in backscatter, modeled with a Mie phase function, gave $r_{\rm eff} \geqslant$ 0.63 μm. A third set of spokes, viewed in forward scatter, indicated $r_{\rm eff} > 0.59$ μm. The sign of the slope of extinction efficiency $Q_{\rm eff}$ with size parameter $x = 2\pi r_{\rm eff}/\lambda$, where λ is the wavelength of observation, suggested that the effective size of spoke particles was about 0.6 μm, and the steepness of the slope indicated that the size distribu-

tion could be rather narrow (Doyle, 1987; Doyle and Grün, 1990).

The robustness of these conclusions was restricted primarily by the limited wavelength coverage of the Voyager blue-sensitive vidicon imaging system. In Doyle and Grün's (1990) models, all of the measurements were on the short wavelength side of the peak of the Mie scattering efficiency curve. The broad wavelength coverage and high photometric accuracy of WFPC2 have enabled us to extend their results to the near-IR. We have measured the wavelength dependence of the contrast of a single dark, isolated spoke observed on the morning (east) ansa on 10 January 1997 in six filters (F336W, F439W, F555W, F675W, F814W, and F785L). To account for orbital motion over the 15-minute duration of the observations, we evolved the images to a common epoch, as described previously and illustrated in Fig. 4. We measured the average $(I/F)_{\text{spoke}}$ near the darkest part of the spoke, and $(I/F)_{\text{B}}$ from the spoke-free ring brightness in the opposite quadrant of the east ansa, at the same relative longitude from elongation. We assume that the B ring material itself in the spoke region has the same photometric properties as the adjacent spoke-free B ring. Doyle and Grün (1990) discuss the minor effects that result from taking into account possible differences between the two. The results are shown in Fig. 5. In the top panel, the spoke and B ring reflectivities are plotted separately. The overall ring spectrum is quite red (Cuzzi et al., 2002), and the spoke is darker than the B ring at all wavelengths. In the bottom panel, we plot the measured spoke contrast magnitude $|\Delta(I/F)/(I/F)_{\text{B}}|$ as a function of the Mie size parameter, $x = 2\pi r_{\text{eff}}/\lambda$, assuming $r_{\text{eff}} = 0.57$ μm (see below). There is a clear peaked shape to the spoke contrast.

For ease of comparison, we follow Doyle and Grün's (1990) approach in modeling the extinction efficiency. We assume that the spoke particles are lossless Mie scattering water ice spheres with a real component of the refractive index equal to 1.33 and a Hansen–Hovenier size distribution given by

$$n(r) = Cr^{(1-3b)/b} e^{-r/r_{\text{eff}}b}, \tag{3}$$

where C is a constant, r is the particle radius, r_{eff} is the effective radius of the distribution, and b is the effective variance (see Doyle and Grün, 1990, Eq. (10), et seq.). The overall particle optical depth is defined by

$$\tau_{\text{dust}} = \int_{r_{\text{min}}}^{r_{\text{max}}} n(r)\pi r^2 Q_e(r,\lambda)\, dr, \tag{4}$$

where $n(r)\,dr$ is the number of particles per unit area, as given by Eq. (3), and $Q_e(r,\lambda)$ is the wavelength-dependent extinction efficiency due to both scattering and absorption.

Using a grid search, we determined r_{eff} and b that gave the best fit to the observed wavelength-dependent spoke contrast in Fig. 5. We assumed that the spoke contrast is proportional to τ_{dust} at each wavelength, and that the constant C in Eq. (3) could be freely adjusted to give the best match to the measurements, which are given in Table 2. We find $r_{\text{eff}} = 0.57 \pm 0.05$ μm and $b = 0.09 \pm 0.03$, the values used for the smooth curve overplotted on the observations. For

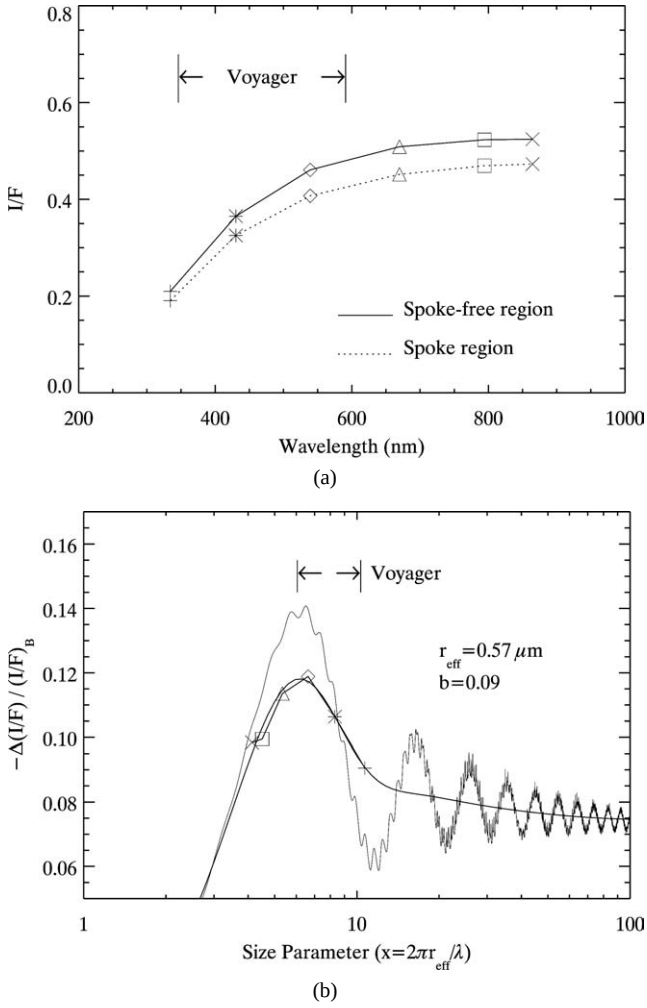

Fig. 5. Photometry of the large, isolated spoke observed on 10 January 1997 shown in Fig. 4. In the upper panel, the I/F of the spoke and of a comparable spoke-free region are shown as a function of the effective wavelength of six broadband WFPC2 filters (F336W, F439W, F555W, F675W, F814W, and F785L). The wavelength coverage of the Voyager spoke observations is much more limited (Doyle and Grün, 1990), as shown by the range demarcated by arrows. The lower panel shows the corresponding spoke contrast magnitude as a function of Mie particle size parameter. The best fitting scaled Mie scattering efficiency for lossless icy spherical particles is overplotted on the observations. For comparison, the Mie extinction efficiency curve for icy spheres is also shown.

Table 2
Spoke photometry

Filter	λ_{eff} (nm)	$(I/F)_{\text{spoke}}$	$(I/F)_{\text{B}}$	$-\Delta(I/F)/(I/F)_{\text{B}}$	Size parameter
F336W	334.3	0.1907	0.2101	0.0905	10.69
F439W	430.3	0.3247	0.3655	0.1064	8.31
F555W	539.2	0.4064	0.4605	0.1189	6.63
F675W	669.7	0.4507	0.5083	0.1136	5.34
F814W	794.2	0.4704	0.5234	0.0994	4.50
F785LP	864.7	0.4726	0.5242	0.0984	4.13

comparison, we also show the Mie scattering function for a monodispersion. The characteristic fringes of the extinction curve are largely suppressed by averaging over the particle size distribution. Our results confirm Doyle and Grün's (1990) finding: the effective spoke particle size is of order 0.6 μm and the size distribution is rather narrow, extending over much less than a decade about $r_{\rm eff}$. As shown in Fig. 5, the Voyager data were restricted to wavelengths below 600 nm and to a size parameter range $0.8 < \log x < 1.1$ ($6.3 < x < 12.6$). In contrast, the HST observations nicely sample both sides of the peak in the scattering efficiency curve.

Our quoted uncertainties in $r_{\rm eff}$ and b reflect the variation in fitted values resulting from assuming different regions to define the spoke boundary. We explored a number of different approaches, such as choosing the darkest region of the spoke, identifying a "region of interest" that defined a contour boundary of the spoke, and using a variety of photometric apertures. The primary challenge was to find a uniform spoke-free region for all filters, taking account of the motion of the spoke between exposures. For most high-contrast spokes, the rings were so highly populated with spokes that a convincingly spoke-free region was difficult to find. The spoke used for this photometric study was exceptional, being dark and isolated, with a spoke-free region for comparison in the opposite quadrant on the same ansa.

We have assumed that the spoke particles are lossless scatterers. For absorbing particles, the amplitude of the fringes in the extinction efficiency curve is reduced, and the high-frequency structure is suppressed. As Doyle and Grün (1990) show, the scattering extinction is much larger than the absorption extinction for plausible compositions, and a refractive index of ice of $1.33 + 0.1i$ (i.e., with a very large and strongly wavelength-dependent imaginary component) would be required to mimic the effects of a very narrow size distribution. To determine the sensitivity of our results to absorption, we fitted the spoke contrast measurements in Fig. 5 to models of lossy ice particles with imaginary parts of the index of refraction of $0.01i$, $0.05i$, and $0.1i$, and we determined the characteristics of the best-fitting Hansen–Hovenier size distribution for each case. The effective particle size was almost unchanged: we found $r_{\rm eff} = 0.568$, 0.550, and 0.536 μm, respectively, for these cases. On the other hand, since absorption and a broad particle size distribution both act to flatten the extinction efficiency curve, the fitted particle size distribution was narrower as the particles became more absorbing. We found $b = 0.08$, 0.03, and 0.01 for the three cases. Thus, our conclusions about the effective spoke particle radius and narrow size distribution hold even for absorbing particles.

The spoke particles appear to have sizes comparable to the icy grains that comprise Saturn's tenuous E ring, the only known ring believed to have a narrow size distribution. The E ring's blue spectrum implies that the ring particles have radii of about ~ 1 μm (Showalter et al., 1991; Nicholson et al., 1996). For both spokes and the E ring, impacts onto the B ring and onto Saturn's mid-sized moons, respectively, probably liberate grains with a wide range of sizes, but only particles near a particular size can stray far from where they are produced. However, the physics involved is different in the two cases (Goertz, 1984; Horanyi et al., 1992; Hamilton and Burns, 1994). We emphasize that the "dust" in the spokes is not the meteoritic material fragmented or vaporized on impact, but is predominantly water ice from the B ring itself. As pointed out by Ćuk et al. (2000), the formation rate of spokes is consistent with the impact rate for 10-kg meteoroids, whereas the mass of material in a spoke is orders of magnitudes larger (Grün et al., 1983).

4. Spoke contrast, detection limits, and haze models

We took a census of spokes in all of our images by measuring the spoke contrast of each recognizably distinct spoke in the F555W images for each HST visit. We defined $(I/F)_{\rm spoke}$ to be the darkest pixel in a given spoke, and $(I/F)_{\rm B}$ to be the typical spoke-free B ring reflectivity at the same orbital radius. The results are shown in Fig. 6. In Table 1, we list the number of spokes seen on each date, separately for the east and west ansae. In all, we identified 36 spokes or spoke complexes. We also tabulate the contrast of the darkest spoke in each visit, for each ansa. In cases where no spokes were visible, we indicate a detection limit given by $0.005/(I/F)_{\rm B}$ ($\simeq 1\%$ in spoke contrast), where $0.005 = -\Delta(I/F)$ for the faintest spoke we could convincingly detect. Generally, spokes were both darker and more abundant on the morning (east) ansa, as was the case for Voyager spokes as well (Porco and Danielson, 1982).

The abundance of detectable spokes decreased sharply with increased ring opening angle in our HST images. To understand why spokes become harder to detect as the rings open up, we have performed multiple-scattering calculations for three plausible distributions of spoke material: (1) the spoke dust is uniformly mixed with the B ring itself; (2) the dust occupies an extended, uniform haze layer, thicker than and centered on the edge-on B ring; and (3) spoke dust lies entirely above the B ring in a uniform haze layer. We describe the results of each of these calculations in turn.

We begin by assuming that the spoke material is embedded within the B ring itself, which is implicit in Doyle and Grün's (1990) radiative transfer development. For this case, we have used classical multiple-scattering ("doubling") models of the B ring, in which the thickness of the layer containing the ring particles is many times the size of the macroscopic particles. In reality, the ring particles have a broad size distribution extending from radii of 0.3 to 20 m (French and Nicholson, 2000), and the ring thickness is probably only a few times the size of the largest particles (Cuzzi et al., 1979; Salo and Karjalainen, 2003). Nonetheless, classical models provide a reasonable point of departure for comparison with our observations. We also assume that the only difference between spoke and non-

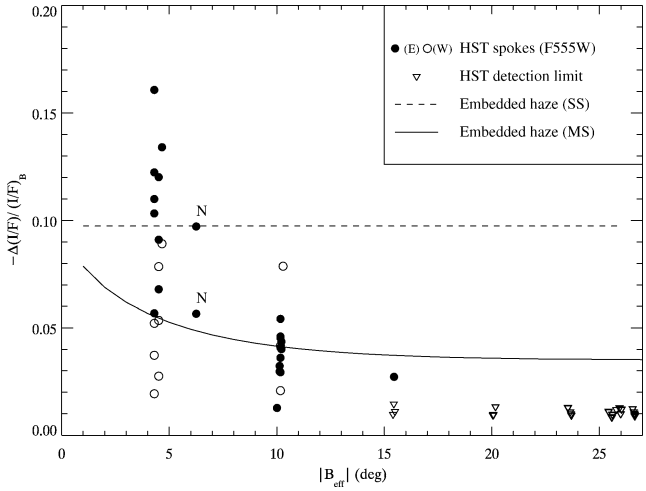

(a)

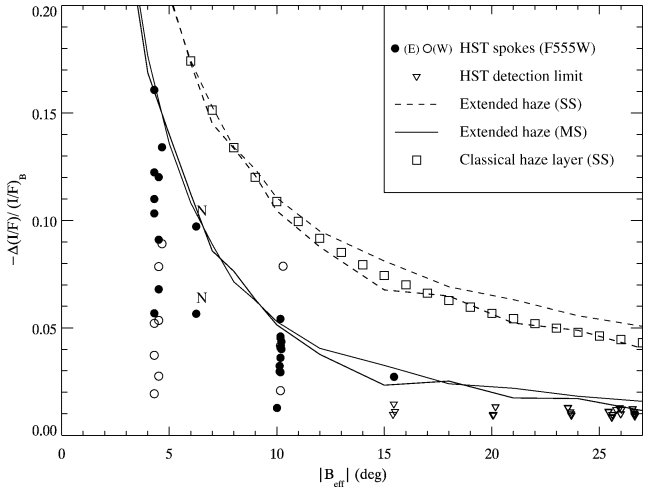

(b)

Fig. 6. (a) A census of spokes detected in HST images from 1994 to 2004. The normalized F555W contrast of each spoke is plotted as a function of effective ring opening angle $|B_{\rm eff}|$. Spokes are generally darker and more numerous on the east (morning) ansa (filled circles) than the west (evening) ansa (open circles). Points annotated by 'N' were observed in wide-field images with the F547M filter on the north face of the rings in 1994, prior to the most recent ring plane crossing epoch. Inverted triangles denote detection limits in cases where no spokes were seen. When the spoke particles are uniformly mixed with the B ring itself, single-scattering (SS) calculations for spoke optical depth $\tau_{\rm dust} = 0.1$ (dashed line) predict no variation in spoke contrast with changing ring opening angle. When multiple scattering (MS) is taken into account, the spoke contrast decreases with $|B_{\rm eff}|$ (solid line), although not as rapidly as suggested by the observations that indicate an absence of detected spokes for $|B_{\rm eff}| > 16°$. (b) Comparison of observations with Monte Carlo simulations of spoke material distributed in an extended haze layer with $\tau_{\rm dust} = 0.04$ that is twice the vertical thickness of the B ring (thin lines), and for a $\tau_{\rm dust} = 0.01$ haze layer lying completely above the B ring (thick lines). Single scattering results are shown dashed, which are well-matched by the simple $(1 - e^{-2\tau_{\rm dust}/\sin B_{\rm eff}})$ behavior expected for a classical haze layer, shown as open squares. Multiple scattering results are shown as solid lines, which match the envelope of spoke observations quite well.

spoke regions is that the former contain microscopic particles having the same spatial distribution as the macroscopic particles. By contrast, Doyle et al. (1989) and Doyle and Grün (1990) assumed that macroscopic particles in spoke and non-spoke regions also have different albedos and phase functions.

In Fig. 6a, we plot the model results obtained when we took the difference between two doubling calculations, one in which $f = 10\%$ of the optical depth of the B ring was comprised of spoke particles, and a second with no spoke particles. We assumed $B = B'$ in steps of 1° up to 27° and a solar phase angle of 1°, which is the median phase angle for our observations. For these calculations we took the spoke particles to be lossless spheres of water ice with a refractive index $1.33 + 0i$. The doubling calculations were performed with the code described by Showalter et al. (1992) and Dones et al. (1993). The large particles in the B ring were assumed to have a backscattering phase function like that of the galilean satellite Callisto (Domingue and Verbiscer, 1997) and a Bond albedo of 0.649, which is appropriate for the F555W filter. The spoke particles had a Hansen–Hovenier size distribution with $r_{\rm eff} = 0.57$ μm and $b = 0.09$, as we found in Section 3. We assumed a single-scattering albedo of 1 and a forward-scattering phase function, calculated with Michael Mishchenko's Mie code spher.f (http://www.giss.nasa.gov/~crmim/brf/), with a Henyey–Greenstein asymmetry parameter, g, of 0.824. In the case in which $f = 10\%$ is assumed, the effective albedo of the ring particles was $(1 - f) \times 0.649 + f \times 1 = 0.684$.

In Fig. 6a, the horizontal dashed line shows the expected fractional change in I/F when only single scattering is considered. In this case it can be shown that if the spoke particles are highly forward-scattering (or have small albedos, which is not the case here), $|\Delta(I/F)/(I/F)_{\rm B}| \to f$. In fact, we find that the fractional decrease is 9.7%, independent of tilt angle, so $|\Delta(I/F)/(I/F)_{\rm B}|$ is indeed nearly equal to f. When multiple scattering is included (solid curve), the contrast is smaller, because some of the multiply-scattered light is scattered back in the direction of the observer. Multiple scattering is larger in the case in which dust is present, both because the effective albedo of the rings is larger and because light is scattered deeper into the ring layer. Multiple scattering also increases more rapidly with tilt angle for $|B_{\rm eff}| \leqslant 15°$ when dust is present. The predicted contrast decreases from 7.9% at $|B_{\rm eff}| = 1°$ to 3.7% at $|B_{\rm eff}| = 15°$, and then remains nearly constant at larger ring opening angles, reaching 3.5% at $|B_{\rm eff}| = 27°$. Our numerical results can be fit to within 10% by the expression $\Delta(I/F)/(I/F)_{\rm B} = -0.023 - 0.061/\sqrt{|B_{\rm eff}|}$, where here $B_{\rm eff}$ is measured in degrees. This decline with tilt angle is much shallower than the measured trend of spoke contrast with tilt angle. We have also performed multiple-scattering calculations in which the spoke particles were assumed to be lossy (imaginary index of refraction as large as 0.1), or in which the spoke particles had an isotropic phase function, as would be expected if the spoke particles were tiny Rayleigh scatterers or larger composite particles. In no case did the embedded haze layer models predict the contrast between spoke and non-spoke regions to vary as rapidly with tilt angle as we observed.

The embedded haze model cannot account for the observed trend.

Next, we determined the predicted spoke contrast for an extended haze layer, thicker than the B ring itself, using the method described by Salo and Karjalainen (2003) and Salo et al. (2004), based on following a large number of photons through a ring composed of discrete finite sized particles. The particle field, with periodic planar boundaries, is illuminated by a parallel beam of photons, and the path of each individual photon is followed in detail from one intersection with a particle surface to the next scattering, until the photon escapes the particle field; the new direction after each scattering is obtained via Monte Carlo sampling of the particle phase function. The brightness at a chosen observing direction is obtained by adding together the contribution of all individual scatterings which are visible from this direction. Compared to a direct Monte Carlo estimate based on tabulating just the directions of emerging photons, this indirect method gives significantly reduced variance of the results.

In the current Monte Carlo models, the particle field is composed of both macroscopic ring particles and dust particles (10,000 in each component), with each of the two components characterized by different phase functions and single scattering albedos as described above for the embedded haze layer models. The optical depth and vertical extent of both components can be varied. Note that using finite sized particles automatically implies shadowing effects, which are absent in classical radiative calculations. In order to make a fair comparison to classical calculations, a small volume filling factor D is used: we assume $D = 0.001$ for the ring particles (and about 3×10^{-6} for the dust), so that the width of the opposition peak $\sim D$ is narrower than the adopted $\alpha = 1°$. Due to the small D the Monte Carlo calculations are very CPU-intensive, since the photons can travel large physical distances between scatterings. In this case, even with 10,000 particles the planar extent of the particle field is much smaller than its vertical extent (about 60 and 1300 particle diameters, respectively). Therefore, especially for low elevation angles, the photon paths typically need to be followed through a large number of periodic copies of the original particle field.

In Fig. 6b, we show the results for two representative Monte Carlo simulations. In the first case, the homogeneous spoke dust layer (with $\tau_{\rm dust} = 0.04$) is centered on, but twice as thick vertically, as the B ring layer of macroscopic ring particles (with $\tau = 2.0$). The predicted effect of ring tilt on spoke contrast, including multiple scattering, is shown as a thin solid line. (The minor undulations in the profile are the result of photon statistics in the Monte Carlo simulations.) The overall trend matches the upper envelope of the measured spokes at low ring opening angles, as well as the detection limits at larger $B_{\rm eff}$. For comparison, the single-scattering results are also shown (thin dashed line). Multiple-scattering reduces the spoke contrast especially effectively at large ring opening angles.

To isolate the effect of an extended haze layer in front of the B ring, we next restricted the spoke material to the upper one-fourth of the previous case. That is, the haze layer had a total optical depth of $\tau_{\rm dust} = 0.01$, with a physical thickness one-half that of the B ring, which lay directly beneath it. The results are shown as the thick lines; they are nearly indistinguishable from the previous Monte Carlo case for the full extended haze layer. As expected, the single-scattering results are matched almost perfectly by the classical expression, $1 - e^{-2\tau_{\rm dust}/|\sin B_{\rm eff}|}$. Collectively, the strong tilt effect on spoke contrast can be accounted for as a result of varying viewing and illumination geometry of an extended layer of dust that lies above the ring itself. A relatively low optical depth ($\tau_{\rm dust} \approx 0.01$) is sufficient to produce the observed contrast. Spoke material within or beneath the B ring itself has little additional effect.

The variation of spoke contrast with ring tilt is strongly dependent on whether the spoke dust extends above the main ring or not. To illustrate the effect of vertical inhomogeneity of the spoke and main ring particles, Fig. 7 shows three panels of the main rings in cross-section: (a) without spoke dust, (b) with spoke dust distributed homogeneously among the cm–m size main ring particles, and (c) with spoke dust distributed in a thicker layer than the main ring particles. By reciprocity, the *reflectance* of the layer (usually denoted R or S)—but not its I/F—is invariant to exchange of source and viewer, even for a vertically inhomogeneous layer (Hovenier, 1969; Hansen and Travis, 1974). Our spoke contrasts are normalized by the background I/F (Eq. (1)), and thus are analogous to reflectance. In all cases, the particle mix traversed by the incoming and outgoing rays determines the average scattering behavior of the observed patch of ring. In the homogeneous case (b), all lines of sight see the same fractional mix of small and large particles regardless of their elevation angle. As the elevation angle increases, the degree of multiple scattering of the reflected light increases, which washes out the contrast between spoke and non-spoke areas (compare the dashed and solid lines in Fig. 6a). However, the difference is small because the effective scattering properties of the layer are not changing with elevation angle.

On the other hand, as shown in the inhomogeneous case (c), if the micron-sized grains are distributed in a thicker layer than the main ring particles, the lines of sight A–B (and B–A) sample a far larger abundance of spoke particles relative to main ring particles, relatively speaking, than lines of sight C–D and D–C. This greatly increases the contrast between spoke- and non-spoke regions relative to that exhibited by the uniformly mixed layer (compare the solid lines in Fig. 6b with those in Fig. 6a). That is, the low optical depth spoke dust is an increasingly dominant contributor to scattered light as the elevation angle decreases, whether the low elevation angle characterizes the illumination, the viewing, or both. It is the dust above, rather than within, the ring that produces the strong tilt effect.

While more modeling is needed, we speculate that the width of the effect in elevation angle is related to the angu-

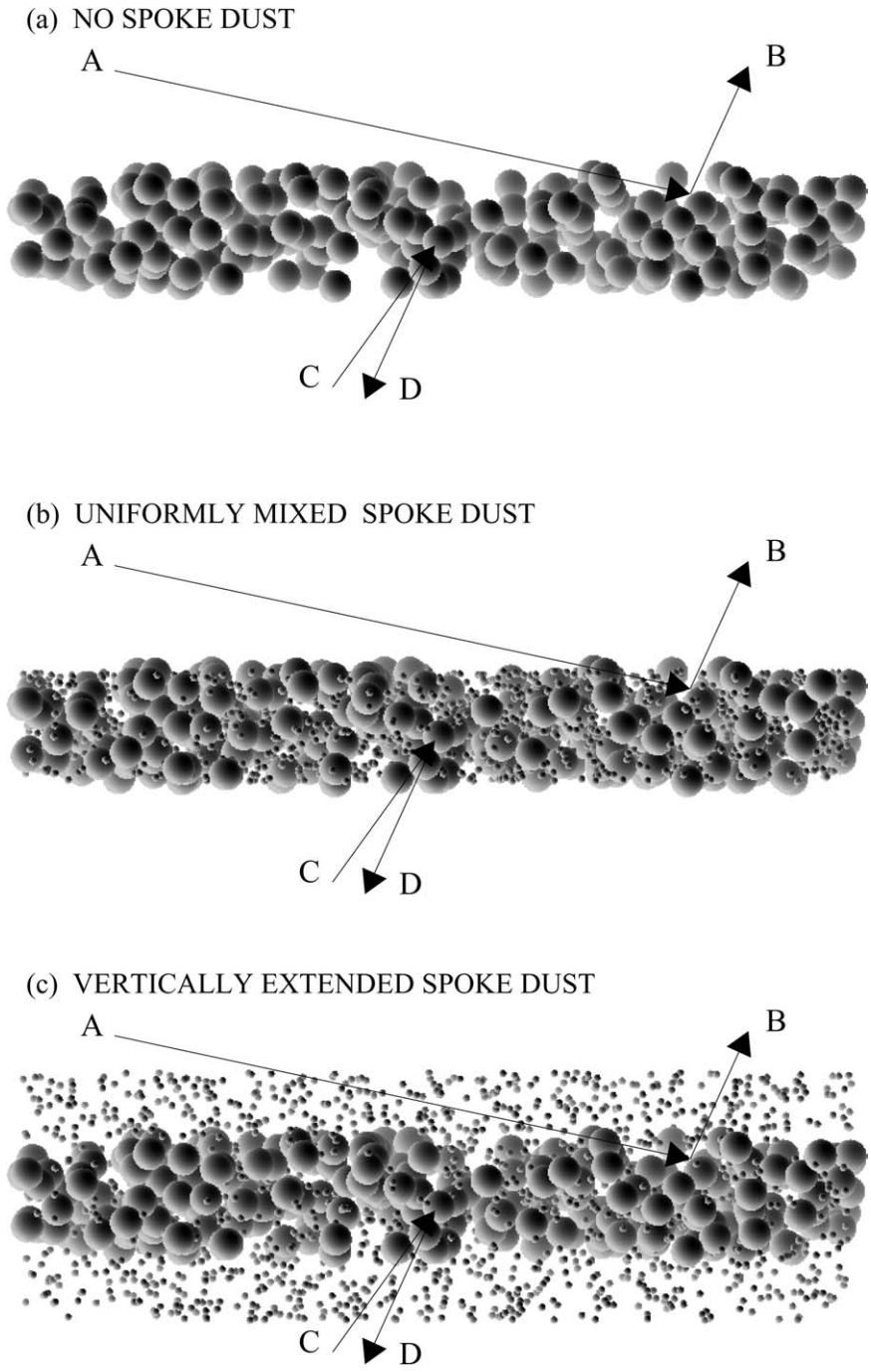

Fig. 7. Cross-section of the B ring (a) in the absence of spoke material, (b) with dust uniformly mixed with the macroscopic ring particles, and (c) with a vertically extended layer of spoke material. Arrows represent lines of sight from the Sun to the observer (or vice versa, by symmetry), after scattering from a B ring particle. In the A–B pair, one line of sight (A) is at a grazing angle relative to the rings, similar to the geometry of the Voyager encounters and the early (1994–1998) HST observations. For the C–D pair, neither line of sight is at grazing incidence, similar to the more recent (1998–2004) HST observations and the early Cassini (mid-2004) observations. See text for additional discussion.

lar width of the spoke particle phase function. That is, if the elevation angle is larger than the typical diffraction lobe extent of a spoke particle, all the light scattered by that particle goes into the ring and, conversely, on emergence, the spoke cloud is as likely to scatter light into the detector as out of it. Ultimately this might be another testable aspect of our hypothesis. Previous models which assumed uniformly mixed dust (Doyle and Grün, 1990) suggested that spoke dust could have optical depth of a few percent; we find that a smaller fraction (about a percent), but inhomogeneously mixed, can match both the detections and non-detections.

The Voyager epoch was characterized by geometry like A–B, in which the Sun had low elevation and the viewer's elevation varied through a large range. From HST, of course,

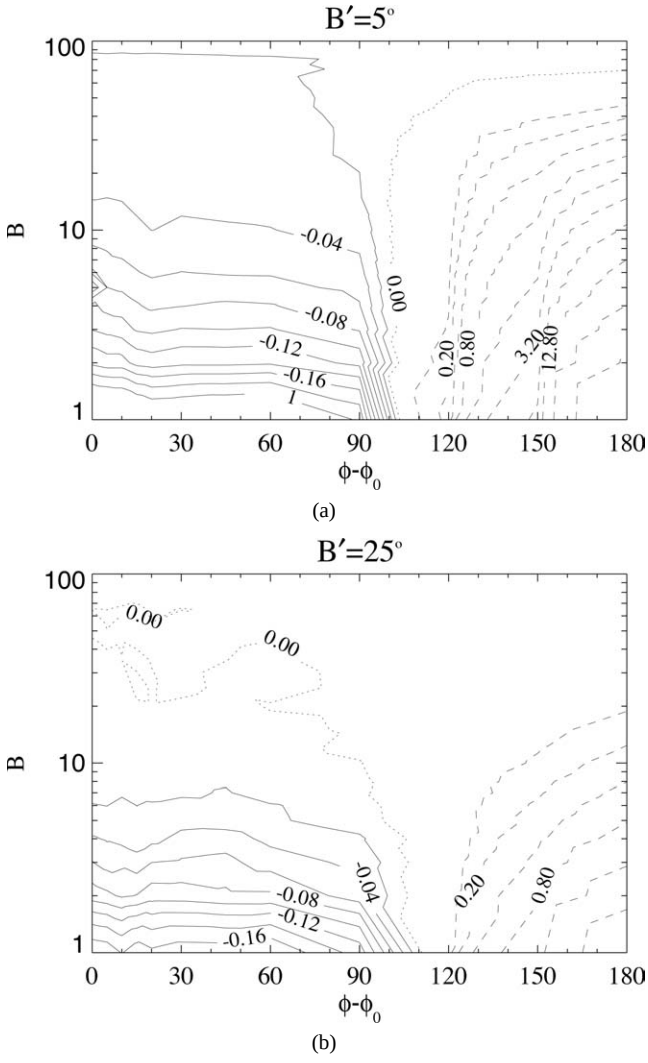

Fig. 8. Contours of spoke contrast, $\Delta(I/F)/(I/F)_{\rm B}$, as a function of ring opening angle B (plotted logarithmically) and azimuth difference $\phi - \phi_0$ between the observer and the source of illumination, for two solar incidence angles, $B' = 5°$ (top) and $B' = 25°$ (bottom). For grazing illumination geometry ($B' = 5°$), spokes have high contrast in both backscatter ($0 \leqslant \phi - \phi_0 \ll 90°$), where they are darker than the surrounding B ring (i.e., the contrast is negative) and in forward scatter ($90° \ll \phi - \phi_0 \leqslant 180°$) where spokes are much brighter than the B ring. Contour intervals are linear for negative contrasts and exponential for positive contrasts. For $B' = 25°$, the predicted contrast is more muted in both forward- and backscatter.

the elevations of the Sun and the viewer are closely tied, and spokes were never seen in C–D or D–C geometries. During most of the Cassini mission, the Sun has moderately high elevation angle so the only geometry in which one might hope to see spokes is when the spacecraft is in a fairly low elevation angle (B–A). We can quantify this with predictions from our Monte Carlo results, which are applicable over the full range of possible illumination and viewing geometries. Figure 8 shows the predicted variations in the spoke contrast as a function of the viewing elevation B and the azimuth difference of the observer with respect to illumination ($\phi - \phi_0$) for two different illumination angles, $B' = 5°$ and $B' = 25°$. The latter corresponds to the current (2004) geometry, while the more shallow illumination approximates the geometry during the Voyager flybys. The solar phase angle α is related to the azimuth difference ($\phi - \phi_0$), B, and B' by

$$\cos(\alpha) = \mu\mu_0 + \sqrt{(1-\mu^2)(1-\mu_0^2)} \times \cos(\phi - \phi_0), \qquad (5)$$

where $\mu = 1/|\sin B|$ and $\mu_0 = 1/|\sin B'|$ (Hansen and Travis, 1974). The solid contours indicate the domain where spokes are viewed in backscatter, and appear dark against their surroundings, while the dashed contours indicate the forward scattering domain where spokes are expected to appear bright. For these calculations, the extended haze model was identical to the $\tau_{\rm dust} = 0.04$ case in Fig. 6b, except that $D = 0.1$ was used instead of $D = 0.001$, in order to speed up the calculations. This is effectively identical to a haze layer with $\tau_{\rm dust} = 0.01$ directly above the main ring.

In the top panel of Fig. 8, the predicted spoke contrast is substantial (-0.04) for ring tilts of $B < 10°$ and $\phi - \phi_0 < 90°$. At this grazing geometry in forward scattering, spokes are extremely bright compared to the B ring, even for quite large ring opening angles ($B \sim 20°$). These results are consistent with Voyager and pre-1998 HST observations. In the lower panel, the reduced spoke contrast with increasing B' is clearly evident. For typical spoke optical depths ($\tau_{\rm dust} \sim 0.01$) and $B' = 25°$, spoke contrast in backscatter will reach -0.04 only for $B < 4°$ (i.e., for quite grazing viewing geometry). If the Cassini detection limit is comparable to our HST value of 0.01, then spokes should be detectable in backscatter for $B < 10°$ and in forward scatter at even larger opening angles.

The details of these calculations depend, of course, on the assumed phase functions of the ring and dust particles. The expected wealth of spoke measurements from Cassini, complemented by the HST data, should make it possible to determine the spoke particle properties much more precisely.

5. Conclusions

From a decade of multiwavelength HST observations, spanning the full range of ring tilt and solar phase angles visible from the Earth, we have detected 36 spokes or spoke complexes in Saturn's B ring. From the wavelength dependence of the spoke contrast, we find that the particle size distribution for a prominent, isolated spoke is quite narrow, with an effective particle size $r_{\rm eff} = 0.57 \pm 0.05$ μm. The photometric contrast of the spokes varies quite markedly with $B_{\rm eff}$: at grazing incidence (and viewing) angle, spokes were prominent, but no spokes were seen between late October 1998 ($B_{\rm eff} = -15.43°$) and March 2004, by which time the rings had reached their maximum opening angle ($B_{\rm eff} = -26.7°$). This effect is well-matched both qualitatively and quantitatively by multiple-scattering calculations for spoke particles in an extended haze layer above the B ring, with optical depth $\tau_{\rm dust} = 0.01$. The results are nearly identical for a haze layer twice as thick as the B ring with total optical depth $\tau_{\rm dust} = 0.04$. It is the amount of dust *above*

the ring that controls the contrast of spokes. When the spoke particles are uniformly mixed with the B ring, multiple scattering results predict a diminished contrast as the rings open, but this model cannot account for the complete absence of spokes with fractional contrast $\geqslant 1\%$ for $|B_{\rm eff}| > 16°$. Additionally, the uniform haze model requires a substantially larger haze optical depth ($\tau_{\rm dust} \approx 0.1$) to match the observed spoke contrast at low ring opening angles.

We conclude that the absence of spoke detections in the post-1998 HST observations, and in the Cassini observations during approach to Saturn (mid-2004), can be attributed to illumination and viewing geometry. Earth-bound observers restricted to $B \sim B'$ will likely have to wait for the rings to close down before spokes are again visible. On the other hand, spokes should be easily detected, albeit rather foreshortened, by Cassini instruments in both forward- and backscatter when the spacecraft approaches ring plane crossing. Over the course of the Cassini orbital tour, spokes should gradually become more visible with the approach of Saturn equinox. Seasonal effects may play a role as well: Cuzzi and Durisen (1990) proposed that spokes are produced by the highest speed impacts onto the rings, whose rate could vary due to Saturn's obliquity as the planet orbits the Sun.

These HST observations, the highest quality long-term Earth-based spoke measurements, provide an important backdrop to the Cassini mission. They sample the full range of solar incidence angles over a full Saturn season (southern spring to summer), for more than twice the duration of the nominal Cassini orbital tour. The Cassini orbiter's multispectral, high resolution images of spokes taken over a wide range of solar phase, incidence, and emission angles should add enormously to our detailed understanding of the origin, evolution, and physical characteristics of spokes (Porco et al., 2004).

Acknowledgments

We thank Michael Mishchenko for the use of his Mie scattering code. Amy Simon-Miller and an anonymous referee provided prompt and useful reviews. Our results are based on observations with the NASA/ESA Hubble Space Telescope, obtained at the Space Telescope Science Institute (STScI), which is operated by the Association of Universities for Research in Astronomy, Inc. under NASA contract No. NAS5-26555. This work was supported in part by STScI Grants GO-06806.01-95A and GO-08660.01A, by NASA's Planetary Geology and Geophysics program under Grants NAG5-4046, NAG5-10197, NAG5-9141, and RTOP 344-30-50-01 and RTOP 344-30-51-02, and by the Academy of Finland.

References

Alexander, A.F.O., 1962. The Planet Saturn: A History of Observation, Theory, and Discovery. Macmillan, New York.

Bastin, J.A., 1981. Note on the rings of Saturn. Moon Planets 24, 467.

Carbary, J.F., Bythrow, P.F., Mitchell, D.G., 1982. The spokes in Saturn's rings—a new approach. Geophys. Res. Let. 9, 420–422.

Colas, F., Frappa, E., Gomez, J., Laques, P., Lecacheaux, J., Tagger, M., 1995. Saturn. IAU Circ. 6129.

Collins, S.A., Cook, A.F., Cuzzi, J.N., Danielson, G.E., Hunt, G.E., Johnson, T.V., Morrison, D., Owen, T., Pollack, J.B., Smith, B.A., Terrile, R.J., 1980. First Voyager view of the rings of Saturn. Nature 288, 439–442.

Connerney, J.E.P., 1986. Magnetic connection for Saturn's rings and atmosphere. Geophys. Res. Lett. 13, 773–776.

Ćuk, M., Burns, J.A., Cuzzi, J.N., Sugita, S., 2000. Will Cassini detect meteors in Saturn's rings? Bull. Am. Astron. Soc. 32, 1087. Abstract.

Cuzzi, J.N., Durisen, R.H., 1990. Bombardment of planetary rings by meteoroids—general formulation and effects of Oort cloud projectiles. Icarus 84, 467–501.

Cuzzi, J.N., Durisen, R.H., Burns, J.A., Hamill, P., 1979. The vertical structure and thickness of Saturn's rings. Icarus 38, 54–68.

Cuzzi, J.N., French, R.G., Dones, L., 2002. HST multicolor (255–1042 nm) photometry of Saturn's main rings. I. Radial profiles, phase and tilt variations, and regional spectra. Icarus 158, 199–223.

Davydov, V.D., 1982. Arguments for the ordered orientation of particles in the Saturn rings and for spokes as a manifestation of magnetic anomalies. Kosmicheskie Issledovaniia 20, 460–471. In Russian.

Domingue, D., Verbiscer, A., 1997. Re-analysis of the solar phase curves of the icy galilean satellites. Icarus 128, 49–74.

Dones, L., Cuzzi, J.N., Showalter, M.R., 1993. Voyager photometry of Saturn's A ring. Icarus 105, 184–215.

Doyle, L.R., 1987. Voyager imaging photometry and radiative transfer modeling of the spoke-like features in Saturn's outer B ring. PhD dissertation. Heidelberg University, Germany.

Doyle, L.R., Dones, L., Cuzzi, J.N., 1989. Radiative transfer modeling of Saturn's outer B ring. Icarus 80, 104–135.

Doyle, L.R., Grün, E., 1990. Radiative transfer modeling constraints on the size of spoke particles in Saturn's rings. Icarus 85, 168–190.

French, R.G., Nicholson, P.D., 2000. Saturn's rings II. Particle sizes inferred from stellar occultation data. Icarus 145, 502–523.

French, R.G., McGhee, C.A., Dones, L., Lissauer, J.J., 2003. Saturn's wayward shepherds: the peregrinations of Prometheus and Pandora. Icarus 162, 143–170.

Goertz, C.K., 1984. Formation of Saturn's spokes. In: COSPAR topical meeting on dust in space and comets, Graz, Austria, June 25–July 7, 1984, Adv. Space Res. 4, 137–141.

Goertz, C.K., Morfill, G., 1983. A model for the formation of spokes in Saturn's rings. Icarus 53, 219–229.

Gold, T., 1980. Electric origin of spokes seen in Saturn's rings. In: Meeting on Planetary Exploration, November 1980. Royal Soc. London, London, England.

Grün, E., Morfill, G.E., Terrile, R.J., Johnson, T.V., Schwehm, G., 1983. The evolution of spokes in Saturn's B ring. Icarus 54, 227–252.

Grün, E., Goertz, C.K., Morfill, G.E., Havnes, O., 1992. Statistics of Saturn's spokes. Icarus 99, 191–201.

Hamilton, D.P., Burns, J.A., 1994. Origin of Saturn's E ring: self-sustained, naturally. Science 264, 550–553.

Hansen, J.E., Travis, L.D., 1974. Light scattering in planetary atmospheres. Space Sci. Rev. 16, 577–610.

Hill, J.R., Mendis, D.A., 1981. On the braids and spokes in Saturn's ring system. Moon Planets 24, 431–436.

Hovenier, J., 1969. Symmetry relationships for scattering of polarized light in a slab of randomly oriented particles. J. Atmos. Sci. 26, 488–499.

Horanyi, M., Burns, J.A., Hamilton, D.P., 1992. The dynamics of Saturn's E ring particles. Icarus 97, 248–259.

Mendis, D.A., Hill, J.R., Ip, W.-H., Goertz, C.K., Grün, E., 1984. Electrodynamic processes in the ring system of Saturn. In: Gehrels, T., Matthews, M.S. (Eds.), Saturn. Univ. of Arizona Press, Tucson, pp. 546–589.

Meyer-Vernet, N., 1984. Some constraints on particles in Saturn's spokes. Icarus 57, 422–431.

Nicholson, P.D., Showalter, M.R., Dones, L., French, R.G., Larson, S.M., Lissauer, J.J., McGhee, C.A., Seitzer, P., Sicardy, B., Danielson, G.E., 1996. Observations of Saturn's ring-plane crossings in August and November 1995. Science 272, 509–515.

Porco, C.C., Danielson, G.E., 1982. The periodic variation of spokes in Saturn's rings. Astron. J. 97, 826–833.

Porco, C.C., 19 colleagues, 2004. Cassini Imaging Science: instrument characteristics and capabilities and anticipated scientific investigations at Saturn. Space Sci. Rev. In press.

Poulet, F., Cuzzi, J.N., French, R.G., Dones, L., 2002. A study of Saturn's ring phase curves from HST observations. Icarus 158, 224–248.

Robinson, L.J., 1980. Closing in on Saturn. Sky Telescope 60, 481.

Salo, H., Karjalainen, R., 2003. Photometric modeling of Saturn's rings. I. Monte Carlo method and the effect of nonzero volume filling factor. Icarus 164, 428–460.

Salo, H., Karjalainen, R., French, R., 2004. Photometric modeling of Saturn's rings. II. Azimuthal asymmetry in reflected and transmitted light. Icarus 170, 70–90.

Sheehan, W., O'Meara, S.J., 1993. Exotic worlds. Sky Telescope 85, 20–24.

Showalter, M.R., Cuzzi, J.N., Larson, S.M., 1991. Structure and particle properties of Saturn's E ring. Icarus 94, 451–473.

Showalter, M.R., Pollack, J.B., Ockert, M.E., Doyle, L.R., Dalton, J.B., 1992. A photometric study of Saturn's F ring. Icarus 100, 394–411.

Smith, B.A., Soderblom, L., Beebe, R.F., Boyce, J.M., Briggs, G., Bunker, A., Collins, S.A., Hansen, C., Johnson, T.V., Mitchell, J.L., Terrile, R.J., Carr, M.H., Cook, A.F., Cuzzi, J.N., Pollack, J.B., Danielson, G.E., Ingersoll, A.P., Davies, M.E., Hunt, G.E., Masursky, H., Shoemaker, E.M., Morrison, D., Owen, T., Sagan, C., Veverka, J., Strom, R., Suomi, V.E., 1981. Encounter with Saturn—Voyager 1 imaging science results. Science 212, 163–191.

Smith, B.A., Soderblom, L., Batson, R.M., Bridges, P.M., Inge, J.L., Masursky, H., Shoemaker, E., Beebe, R.F., Boyce, J., Briggs, G., Bunker, A., Collins, S.A., Hansen, C., Johnson, T.V., Mitchell, J.L., Terrile, R.J., Cook, A.F., Cuzzi, J.N., Pollack, J.B., Danielson, G.E., Ingersoll, A.P., Davies, M.E., Hunt, G.E., Morrison, D., Owen, T., Sagan, C., Veverka, J., Strom, R., Suomi, V.E., 1982. A new look at the Saturn system—the Voyager 2 images. Science 215, 504–537.

Tagger, M., Henriksen, R.N., Pellat, R., 1991. On the nature of the spokes in Saturn's rings. Icarus 91, 297–314.

Trauger, J.T., Vaughan, A.H., Evans, R.W., Moody, D.C., 1995. Geometry of the WFPC2 focal plane. In: Koratkar, A., Leitherer, C. (Eds.), Calibrating Hubble Space Telescope: Post Servicing Mission. Space Telescope Science Institute, Baltimore, pp. 379–385.